Ultrasonics Sonochemistry 77 (2021) 105679

Contents lists available at ScienceDirect

Ultrasonics Sonochemistry

journal homepage: www.elsevier.com/locate/ultson

Mechanism study of Single-Step synthesis of Fe(core)@Pt(shell) nanoparticles by sonochemistry

Ah-Hyeon Park, Wenjuan Shi, Jong-Un Jung, Young-Uk Kwon *

Department of Chemistry, Sungkyunkwan University, Suwon 16419 Korea

ARTICLE INFO

Keywords:
Electrocatalysis
Sonochemical method
Core–shell nanoparticles
Mass production
Mechanism study

ABSTRACT

Transition metal (TM) core-platinum (Pt) shell nanoparticles (TM@Pt NPs) are attracting a great deal of attention as highly active and durable oxygen reduction reaction (ORR) electrocatalysts of fuel cells and metal-air batteries. However, most of the reported synthesis methods of TM@Pt NPs are multistep in nature, a significant disadvantage for real applications. In this regard, our group has reported a single-step method to synthesize TM@Pt NPs for TM = Mn, Fe, Co, and Ni by using sonochemistry, namely the UPS (ultrasound-assisted polyol synthesis) method. Previously, we proposed the mechanism of the formation of these TM@Pt NPs by UPS method, but rather in a rough sense. Some details are missing and the optimal conditions have not been established. In the present work, we performed detailed studies on the formation mechanism of UPS reaction by using Fe@Pt NPs as the model system. Effects of synthesis parameters such as the nature of metal precursor, conditions of ultrasound, and temperature profile as a function of reaction time were assessed, along with the analyses of intermediates during the UPS reaction. As results, we verified our previously proposed mechanism that, under appropriate conditions, Fe core is formed through the cavitation and implosion of the solvent, induced by the ultrasound, and the Pt shell is formed by the chemical reaction between Fe core and Pt reagent, independent from the direct effect of ultrasound. In addition, we established the optimal conditions to obtain a high purity Fe@Pt NPs in a high yield (>90% based on Pt), which may enable the increase of synthesis scale of Fe@Pt NPs, a necessary step for the real application of TM@Pt NPs.

1. Introduction

Core-shell nanoparticles (NPs) with a transition metal (TM) in the core and platinum (Pt) in the shell (TM@Pt) have a great deal of technological and economical potentials to be used in the field of electrocatalysis [1–3]. Relevant data in the literature show that such core–shell NPs show greatly enhanced performance over pure Pt NPs not only in terms of saving precious Pt but also dramatically decreasing the overpotential through the so-called ligand effect and the strain effect that arise from the interaction between Pt and TM atoms [4–7]. Typically, the oxygen reduction reaction (ORR) on catalysts based on pure Pt NPs shows an overpotential of 0.3 V, which account about 50% of the loss of energy with respect to the theoretical value. Data on core–shell NPs show consistently lower overpotentials by 0.05–0.10 V which can be a significant gain in energy for fuel cells [8,9]. In addition, the Pt shell can provide protection of the inner TM elements, enhancing the durability of the catalysts. These beneficial attributes of TM@Pt NPs seem to make them an ideal candidate to replace the present pure Pt electrocatalyst.

There have been a number of methods developed to synthesize core–shell NPs [10–13]. While some of them have exhibited the potentials to be realized in real applications, the complexity of synthesis processes inherent to their multiple-step procedure has been a problem. In this regard, our group has reported a single-step synthesis method by using sonochemistry, namely, UPS (ultrasound-assisted polyol synthesis) method [14–16]. It is truly single-step in nature because all it takes to form core–shell NPs is to apply an ultrasound for a couple of hours to a polyol solution (typically ethylene glycol, EG) containing metal precursors and carbon as the support. The remaining processes are filtration, washing, and drying. The products can be handled in air because the TM elements in them are well protected by stable Pt shells. Recently, we applied this method to synthesize core–shell NPs with the core composed of a TM element and palladium [17]. Although sonochemistry has been applied to the synthesis or fabrication of energy-related materials in various ways [18–22], the catalyst NPs in all of them are composed of pure Pt. Therefore, our UPS method is distinguished from the rest of sonochemical techniques for its ability to form core–shell NPs

* Corresponding author.
E-mail address: ywkwon@skku.edu (Y.-U. Kwon).

https://doi.org/10.1016/j.ultsonch.2021.105679
Received 16 May 2021; Received in revised form 12 July 2021; Accepted 19 July 2021
Available online 22 July 2021

in single-steps.

In order to form the TM@Pt core–shell structure, a general approach would be to form TM cores (in the form of TM NPs) first and then to form Pt shells on them. Because of the relative reduction potentials of Pt ions and TM ions, this means that TM ions must be reduced in the absence of Pt ions, and then Pt ions are introduced ('redox transmetalation' [23]) with or without an additional reagent depending on the method of reaction chosen. Therefore, to synthesize TM@Pt NPs, at least two separate steps seem to be required. In this sense, the formation of TM@Pt NPs in a single step reaction is counterintuitive.

To answer this puzzle, we have proposed a mechanism that involved the vaporization of precursor molecules into the bubbles that are formed during ultrasonication. While $Pt(acac)_2$ (acac = acetylacetonate), the Pt-precursor we used, is practically non-volatile, acac complexes of TM ions are much more volatile [24,25]. While this mechanism appears to be a logical way to explain the formation of TM@Pt NPs, there remain some many details unknowns.

In the present work, we performed detailed studies on the formation mechanism of TM@Pt by UPS method. Of the four systems with TM = Mn [26], Fe [15], Co [14], and Ni [16] we have reported, we chose TM = Fe system for the mechanism studies because of the following reasons: First, by chance, Fe@Pt system is the most thoroughly investigated, including its 3D structure with the atomic coordinates of all atoms in the model structure based on structural refinements on its high-energy X-ray diffraction pattern [27]. The structure shows that the core is composed of (distorted) body-centered cubic structure of Fe and the shell is of face-centered cubic structure of Pt with well-defined boundary between the core and shell. The model structure could explain not only its enhanced ORR activity but also its magnetic data. Second, $Fe(acac)_3$, the Fe-reagent used in the synthesis of Fe@Pt NPs, shows a strong color not only in the solid state but also in the dissolved state in the solvent during UPS reaction, which contrasts with the other reagents. The strong color of the $Fe(acac)_3$ solution enables one to follow the progress of reaction visually.

Through detailed analyses and elaborate observations of the reaction progress, we propose a refined mechanism for the formation of Fe@Pt NPs through a UPS reaction, which may be deemed to be similar to the previous one. However, there are some important differences between them, which may give different implications. Details are reported below.

2. Experimental section

2.1. Materials

Platinum(II) acetylacetonate ($Pt(acac)_2$, 97%), platinum(II) oxide (PtO_2), iron(III) acetylacetonate ($Fe(acac)_3$, 97%), and iron(II) acetylacetonate ($Fe(acac)_2$, 99.9%) were purchased from Sigma-Aldrich. Commercial Pt/C catalyst (TKK, 37.7 wt% Pt on Vulcan XC-72) was purchased from Premetek. Perchloric acid ($HClO_4$, 70%), ethylene glycol (EG, 99.9%), and ethanol (99.9%) were purchased from Samchun Pure Chemical. Commercial carbon materials, Ketjen Black-300JD (KB; surface area = ~950 $m^2\ g^{-1}$; from Inforchems), Vulcan XC-72 (VC; surface area = ~150 $m^2\ g^{-1}$; from Cabot), and graphite (crystalline, 325 mesh, 99%), were used. Graphene oxide (GO) was synthesized by following the reported so-called improved Hummers method [28]. Reduced graphene oxide (RGO) was obtained by treating GO under a high pressure NH_3 gas (80 bar) at 550 ℃ for 4 h. Partially oxidized KB (KB-oxi) was obtained by following the improved Hummers method to KB in the place of graphite and using an oxidizing solution diluted by 10 fold from the original method. Likewise, partially oxidized VC (VC-oxi) was obtained.

2.2. Syntheses of Fe@Pt /C catalysts

To synthesize Fe@Pt/C electrocatalysts with 40 wt% of Pt loading, we followed the procedure reported previously [15]. Briefly, 0.1 mmol (35.4 mg) of $Fe(acac)_3$, 0.1 mmol (40.5 mg) of $Pt(acac)_2$, and 45 mg of a carbon support were dispersed in 30 mL EG in a 50 mL three-necked container designed for ultrasonication reactions to enable a gas flow while applying ultrasound. The suspension was irradiated by an ultrasound for 3 h by using a high-intensity ultrasonic probe (Sonic and materials, VC-500, 30% amplitude, 20 kHz, with 13 mm solid type probe) while Ar was flown. After the sonochemical reaction, the resultant dark slurry was filtered with a Nylon membrane filter paper with 0.2 μm of pore size (Whatman int. Ltd.) and was thoroughly washed with excess of ethanol. Finally, the obtained samples were dried in a vacuum desiccator at room temperature for 12 h. The yield of Pt was 91.2 ± 3.9 % based on elemental analysis data of five separately synthesized samples.

2.3. Instruments for characterization

X-ray diffraction (XRD) patterns were recorded by using a DC/Max 2000 X-ray diffractometer (Rigaku, Cu Kα (λ = 1.54056 Å)). The gaseous by-products during the sonochemical synthesis of Fe@Pt NPs were identified by using a gas chromatography mass spectrometry (GC/MS, HP 6890 series, Hewlett Packard, Palo Alto, CA, USA). Thermogravimetric data were recorded by using a thermogravimetric analyzer (TGA, Hitachi STA 7200) in air. The elemental compositions of samples were determined by inductively coupled plasma-atomic emission spectroscopy (ICP-AES, Perkin Elmer) and energy dispersive X-ray spectroscopy (EDS) using an EDS analyzer attached on a scanning electron microscope (SEM, JEOL JSM-6700F). Five different spots of each electrocatalyst were measured to obtain averaged compositions. The microstructures and elemental distributions of samples were observed with transmission electron microscopy (TEM, JEOL JEM-3011, 200 kV) and scanning transmission electron microscopy (STEM, JEOL JEM-ARM200F, 200 kV).

3. Results and discussion

In our previous report on the formation of Fe@Pt NPs by UPS method, we proposed a mechanism in which acetaldehyde (CH_3CHO), a decomposition product of EG solvent molecule, functions as the major reducing agent for $Fe(acac)_3$ into Fe^0 [15]. The reason for the formation of Fe core before Pt shell was attributed to the much higher volatility of $Fe(acac)_3$ (vapor pressure of 2.6 hPa at 383 K) [24] than $Pt(acac)_2$ (vapor pressure of 0.5 kPa at 483 K) [25]. Volatile $Fe(acac)_3$ molecules are selectively vaporized and accumulated in the bubbles formed by the action of ultrasound and are reduced into Fe^0 atoms through the reaction with acetaldehyde, which quickly condense into Fe NPs (reactions 1 and 2). On the contrary, nonvolatile $Pt(acac)_2$ molecules are remained outside of bubbles and hence are not given a chance to be reduced. Instead, they undergo galvanic displacement reaction with Fe NPs when they diffuse into the solution. This reaction can be continued until the surface of Fe NPs is fully covered with Pt so that no further galvanic displacement reaction is possible (reaction 3). The result would be Fe@Pt NPs with Pt forming monolayer shells. In fact, we also showed that, by controlling the relative amounts of the reagents, the Pt-shell thickness could be controlled between monolayer to bilayer. This was explained by the deposition of Fe^0 atoms on the Pt shell, through the reaction between $Fe(acac)_3$ and acetaldehyde, which are displaced by additional $Pt(acac)_2$ molecules [29,30].

$$HOCH_2CH_2OH \rightarrow CH_3CHO + H_2O \quad (1)$$

$$CH_3CHO + 2/3\ Fe^{3+} + H_2O \rightarrow CH_3COO^- + 2/3\ Fe^0 + 3H^+ \quad (2)$$

$$Fe_n + x\ Pt(acac)_2 \rightarrow 2x/3\ Fe(acac)_3 + Fe_{n-x}Pt_x\ (=Fe@Pt) \quad (3)$$

While this mechanism explains the counterintuitive formation of Fe@Pt NPs in a single-step, some details are in error. Especially, it does not account the radicals that are formed by the implosion of bubbles

during ultrasonication [31,32]. In addition, the effect of temperature on the reaction progress was not included.

Chemical reactions under ultrasonication are generally explained by the acoustic cavitation mechanism [31,32]. According to this mechanism, the periodic localized compression and expansion of solution by the ultrasound induce bubbles to form and grow in size. After reaching a critical size, the bubbles implode generating high energy pulses. It has been reported that a temperature as high as 5000 K and a pressure as high as 1000 bar can be achieved in a very short time with the decay rate of the pulse as high as 10^9 K s^{-1}. This extremely short-lived high energy pulse can break any chemical bonds, mostly of the solvent molecules, generating radicals. These primary radicals can be the source of various chemical reactions, but most of them are short-lived, while some of them generate longer-lived secondary radicals which diffuse into the solution inducing chemical reactions. The effects of these radicals need to be considered in the formation of Fe@Pt NPs.

The effect of temperature on UPS reactions can be appreciated by the temperature-variation with reaction time in a typical UPS reaction between $Fe(acac)_3$ and $Pt(acac)_2$ (Fe/Pt mole ratio of 1) in Fig. 1. The solution temperature rises continuously during the first ~ 30 min and is held constant afterward. The final temperature, 155 ℃ in this case, is attained by the balance between the heat generated by ultrasonication and the heat dissipated. Many factors can induce deviations from the temperature–time behavior of this figure.

Some notable changes in the appearance of the reacting solution are also shown in this figure. The first notable event is the formation of a clear red–orange solution, which we interpret as the complete dissolution of $Fe(acac)_3$ and $Pt(acac)_2$ reagents. In the following discussion, we will denote this state as state A. The next event is the formation of a murky or turbid solution, which is associated with the formation of Fe NPs (state B). The final visible event is the formation of an opaque black solution, which is the signature of the formation of Fe@Pt NPs (state C). Since the transition from one state to the next one occurs while the solution temperature changes, temperature appears to play an important role in the reaction progress as well as the direct effect from ultrasonication.

3.1. Analysis of gaseous products of ultrasonication

In order to see whether radicals are indeed formed and involved in the formation reaction of Fe@Pt NPs, we identified the gaseous species produced during the synthesis of Fe@Pt. The gaseous species emitted from the reacting solution with 30 min of time intervals were collected and analyzed with GC–MS. Peaks of M/e ratios of 43, 44, 45, and 61 g mol^{-1} were detected in the GC–MS spectra, which could be identified as acetyl, acetaldehyde, 2-hydroxyethyl, and (2-hydroxyethyl)oxidanyl, respectively. The first three can be explained as dehydroxylation products of EG with rearrangement of protons and the last a deprotonation product of EG. Among these, acetyl is the major species, much larger than the rest. These peaks grew with reaction time with no other peaks detected (Figure S1). Because all these species could be explained to be as fragments of EG, their observations are in agreement with the mechanism of sonochemistry in which the first event accompanying the bubble implosion is the bond-breaking of EG solvent molecules. Especially, the abundance of acetyl indicates that the major radical species are formed through the breaking of C–O bonds of EG, mainly in the form of HO· radicals (eqn. 4). The reaction in eqn. 1 may be a consequence of the radical formation. In addition to radicals, the active chemical species such as formaldehyde may function as a reducing agent as shown in eqn. 1 and eqn. 2.

$$HOCH_2CH_2OH\ (M/Z = 62) \rightarrow HOCH_2CH_2\cdot + HO \quad (4)$$

$$HOCH_2CH_2OH\ (M/Z = 62) + HO \rightarrow COCH_3\cdot\ (M/Z = 43) + 2\ H_2O \quad (5)$$

$$HOCH_2CH_2OH\ (M/Z = 62) + H \rightarrow HOCH_2CH\cdot\ (M/Z = 44) + H_3O^+ \quad (6)$$

$$HOCH_2CH_2OH\ (M/Z = 62) \rightarrow HOCH_2CHOH\cdot\ (M/Z = 61) + H \quad (7)$$

$$HOCH_2CH_2OH\ (M/Z = 62) \rightarrow HOCH_2CH_2\cdot\ (M/Z = 45) + OH \quad (8)$$

3.2. Reactions of Pt-reagent under UPS condition

The above described mechanism suggests that the Pt-reagent stays outside of the bubbles. In order to enable the galvanic displacement reaction with Fe^0 atoms on Fe NPs, the Pt-reagents must be homogeneously distributed in the solution and mobile in the solution. In other words, the solubility of the Pt-reagent may affect the synthesis. For this purpose, various platinum halides would be ideal reagents to verify this prediction. Unfortunately, however, halide ions, especially Cl^-, are known to be highly corrosive to the material of the sonicator horn and could not be used in the present study. We, therefore, tried to use PtO_2 in

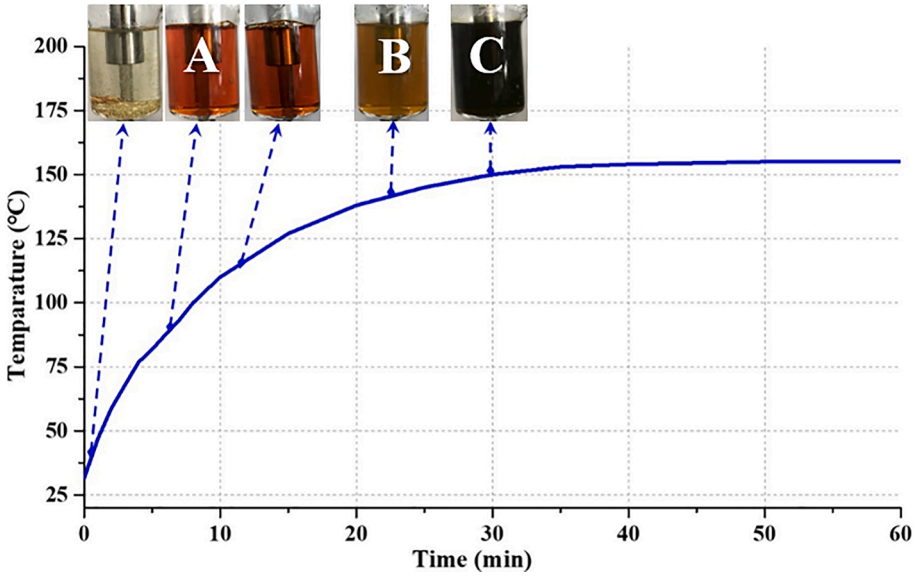

Fig. 1. Temperature variation with reaction time of a UPS reaction between $Fe(acac)_3$ and $Pt(acac)_2$ in EG under continuous ultrasonication with 30% of amplitude. Representative states of the reacting solution, detected by the solution appearance are shown for their time or occurrence.

the place of $Pt(acac)_2$ to see the effect of the solubility of Pt-reagent. PtO_2 is an ionic compound composed of Pt^{2+} and O_2^{2-} ions, because of which it is expected not to dissolve in the EG solvent, contrary to $Pt(acac)_2$ [25]. UPS reaction of an EG solution containing $Pt(acac)_2$ and KB produced Pt NPs, but in a low yield of less than 10% of the initial Pt. By contrast, the same reaction with PtO_2 instead of $Pt(acac)_2$ produced considerably higher yield of Pt NPs (Figure S2). Because both $Pt(acac)_2$ and PtO_2 have very low or no vapor pressure, they are not likely to have any chance to react with the primary radicals, making the reaction with the secondary radicals the only possibility to explain the formation of Pt NPs from these reactions. We, therefore, can explain the different reactivity between PtO_2 and $Pt(acac)_2$ as in the following: Secondary radicals diffuse in the solution and encounter the Pt-reagents. In case of the reaction of PtO_2, its particles are likely to be present as deposited on KB. Reactions with radicals produce Pt atoms on such PtO_2 particles. The accumulation of such results eventually produces Pt NPs on KB. On the contrary, in case of using $Pt(acac)_2$ as the reagent, the soluble molecules are dispersed in the solution. While some of them may undergo reduction reaction with secondary radicals to form Pt^0 atoms, they are well separated from one another decreasing their chance to grow into sizable Pt NPs to be collected on KB.

Interestingly, the yield of Pt NPs from the UPS reaction of $Pt(acac)_2$ can be significantly enhanced by using carbon supports with surface functional groups. When GO was used as the support, a significant amount of Pt NPs could be deposited on the surface of GO. When RGO was used instead, there was practically no Pt NP deposited. We repeated this comparison by using KB, VC, and their derivatives by partially oxidizing their surfaces. (See Supporting Information, Figures S3 and S4, Table S1) The yield of Pt on partially oxidized KB is much larger than on KB. The dependence of Pt yield on support when using $Pt(acac)_2$ may be interpreted as due to the different reaction pathways provided by the functional groups. That is, supports with oxygen functional groups bind $Pt(acac)_2$ molecules on their surface providing heterogeneous nucleation sites for Pt NPs to grow while those without any functional groups do not have such interaction leaving the reaction follow the homogeneous nucleation pathway.

These observations are in good agreement with the above described reaction pathway for $Pt(acac)_2$. When there are few anchoring sites on the substrate, the formation of Pt NPs from $Pt(acac)_2$ is bound to follow the homogeneous nucleation mechanism, where the molecules are dispersed in the solution and have little chance to nucleate Pt seeds to grow into Pt NPs. Contrarily, when a large part of $Pt(acac)_2$ molecules is anchored on the substrate surface, the reaction pathway follows the heterogeneous nucleation pathway. With solid PtO_2, the reduction is bound to occur through the heterogeneous nucleation mechanism, regardless whether the PtO_2 particle is deposited on the carbon support or not, in which case the chance to form Pt NPs is much high compared with the soluble $Pt(acac)_2$ case.

We, then, tried the reaction of PtO_2, instead of $Pt(acac)_2$, with $Fe(acac)_3$ in the presence of KB. In the XRD pattern of the reaction product showed peaks of pure Pt without any hint of Fe incorporation into the Pt lattice. (Figure S5a) Although the elemental composition of the product by EDS showed Fe atoms along with Pt, (Figure S5b) Fe atoms could be readily removed by treating with 0.1 M $HClO_4$ solution, suggesting that Fe in this sample was not protected by Pt as would be expected in Fe@Pt core–shell structure. The same results were obtained when other transition elements such as Mn, Co, and Ni were used. That is, their XRD patterns show peaks closer to that of pure Pt than the corresponding samples obtained by using $Pt(acac)_2$ (Figure S6), indicating the formation of Pt NPs instead of TM@Pt NPs when PtO_2 is used. Therefore, it became evident that the use of PtO_2 did not form Pt-shells on Fe-cores. Instead, the products seem to be best described as a mixture between Pt NPs and Fe-species, most likely to be FeO(OH) based on our previous paper on the UPS reaction of $Fe(acac)_3$ on KB [33,34]. This observation clearly demonstrates that the mobility of Pt reagents is essential for the formation of Fe@Pt core–shell NPs, in agreement with the proposed mechanism.

3.3. Reactions of Fe-reagents under UPS condition

We tried reactions using $Fe(acac)_2$ in the place of $Fe(acac)_3$. (Figure S7) The product of the reaction between $Fe(acac)_2$ and $Pt(acac)_2$ showed some sign of Fe-incorporation into the Pt lattice from their XRD patterns with the peaks of Pt shifted to higher angles from those of pure Pt. The elemental compositions determined by EDS show that the Fe : Pt ratio of Fe(II)@Pt to be 42 : 58, slightly higher in Fe than the Fe : Pt ratio of 35 : 65 in the product from between $Fe(acac)_3$ and $Pt(acac)_2$. The Fe : Pt ratio in the latter agrees with that of the model NP with a monolayer Pt shell and the size of 2.3 nm, obtained from the structural refinement against the XRD data [27]. The higher Fe content in the former implies larger NPs if the monolayer Pt shell is to be maintained, some Fe-species unassociated with Pt, or both. The major contrast between them is observed when the Fe and Pt distributions are compared in a large scale. A large scale EDS map shows that there are regions where Fe atoms are accumulated in the sample, however, which problem is not found in sample from $Fe(acac)_3$. (Figure S7b) The TEM image shows that the particles are not as evenly distributed as in Fe(III)@Pt/C. As shown in the histogram of the particle sizes, the average particle size in Fe(II)@Pt/C is 2.7 $\pm$ 0.6 nm, larger than that in Fe(III)@Pt is 2.3 $\pm$ 0.3 nm. This is mainly because there are some large particles (>3.5 nm) in the former which are absent in the latter. In addition, although a few, very small particles smaller than 1.5 nm in Fe(II)@Pt/C. The observations on the TEM image conclusively indicate that the synthesis with $Fe(acac)_2$ produces a less homogeneous sample than $Fe(acac)_3$, possibly with pure or almost pure Pt NPs mixed. Therefore, we can conclude that the synthesis by using $Fe(acac)_3$ produces more desirable product with mostly Fe@Pt NPs then $Fe(acac)_2$.

These observations appear to be strongly related with the vapor pressures of the Fe-reagents. Contrary to $Fe(acac)_3$, the vapor pressure of $Fe(acac)_2$ cannot be found in the literature. A plausible explanation for the absence of the vapor pressure data on this molecule is that it is non-volatile and has no reason to measure its vapor pressure. In fact, in case of other transition metal complexes of acac ligand, it is established that the complexes of trivalent metal ions are volatile while those of divalent metal ions are not so volatile. The reason for this general observation can be found in their crystal structures. In $M(III)(acac)_3$ complexes, each metal ion can be coordinatively saturated by coordinating to the three bidentate acac ligands around it, making the molecules mononuclear. Therefore, the monomeric complexes can pack into solids. When dissolved in a solution, it is highly likely that their monomeric structures are preserved. By contrast, in case of divalent metal cations, $M(II)(acac)_2$, the required coordination number per cation cannot be satisfied by the two acac ligands in the formula unit. In the crystal structures of these complexes show oligomeric units with bridging acac ligands between two or more M(II) ions. The increased masses of the oligomers make the vapor pressures low, making them less reactive [35,36]. Therefore, there are some Fe NPs formed even after the major part of Pt is consumed. Such Fe NPs do not have the chance to be protected by forming Pt shells. They become Fe oxides or oxy(hydroxide) upon exposure to air during the filtration and washing steps.

3.4. Reactions of $Pt(acac)_2$ and $Fe(acac)_3$ under UPS conditions

We made visual observations on the reaction progress of the formation of Fe@Pt NPs (Fig. 2). Unlike the typical reaction where a carbon support is included, the reaction was run without added carbon for clear visualization. The solution color changes from red-orange to brown and then to black with time. The states A, B, and C mentioned in Fig. 1 are marked in this figure. The initial solution is colorless with a slight red-tint because both $Fe(acac)_3$ and $Pt(acac)_2$ are practically insoluble in EG at room temperature. The red–orange color during the first 10 min after the dissolution of the reagent appears to be due to the color of Fe

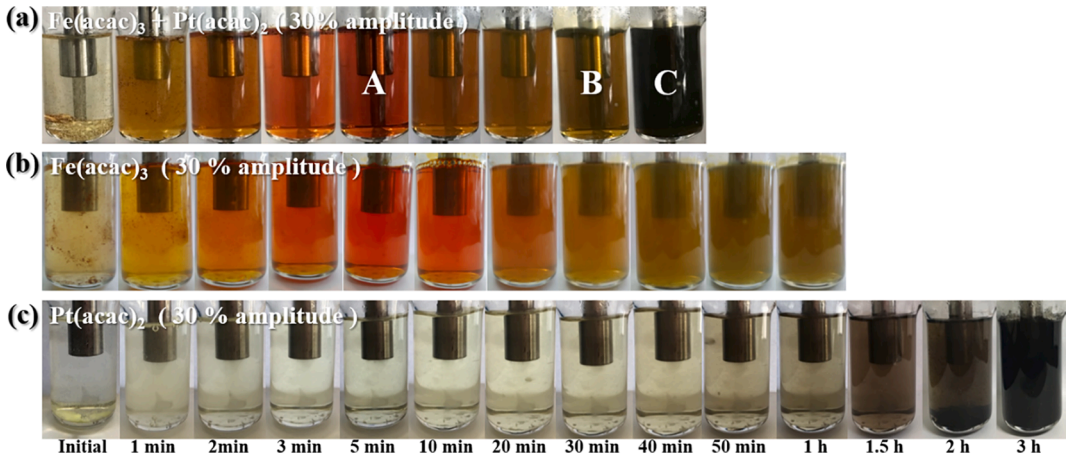

Fig. 2. Visual observations of solutions during UPS reaction in EG. The reagents are (a) $Fe(acac)_3$ and $Pt(acac)_2$ (Fe : Pt = 1 : 1), (b) $Fe(acac)_3$, and (c) $Pt(acac)_2$. State A, B, and C shown in Fig. 1 are marked in (a).

$(acac)_3$ in solution. This can be confirmed by the colors of the other two reactions in Fig. 2 in each of the two precursors was reacted separately under the same condition. The reaction on $Fe(acac)_3$ shows a similar red–orange color as the solution containing both $Fe(acac)_3$ and $Pt(acac)_2$. On the contrary, the solution of $Pt(acac)_2$ remains colorless until about 40 min. The reaction of $Fe(acac)_3$ alone starts to take some turbidity from 20 min and the degree of the turbidity increases with time. However, this solution does not reach the darkness seen in the reaction between $Fe(acac)_3$ and $Pt(acac)_2$. The reaction of $Pt(acac)_2$ hardly shows any change for most of the time. However, at the end of the reaction, the solution starts to take black turbidity. The on-set of the black color in the reaction between $Fe(acac)_3$ and $Pt(acac)_2$ is earlier than the reaction of either reagent alone, suggesting the cooperation between the two reagents, which must be the galvanic displacement reaction.

We followed the reaction progress by taking small aliquots in the course of the reaction and analyzed the solid products for the composition. To do this, we ran a reaction triplicated in the reaction scale from that of the typical reaction in 30 mL EG. Out of the solution of the initial volume of 90 mL, a 5 mL aliquot was taken at every 30 min of reaction until 90 min and then at the end of the reaction after 3 h. In order to make sure that the sampled solution is of the same composition as the other part, the reaction was run without carbon support. To each aliquot, 7.5 mg of KB was added and the solution was stirred for 10 min to induce the deposition of any solid materials on KB. After collecting the solid materials by filtration and washing, the Fe and Pt contents were analyzed by ICP. The results are summarized in Fig. 3a. The curves in this figure can be considered as representing the yields of Fe and Pt in any solid form at the designated time. Since this reaction is proven to produce a high yield of Fe@Pt NPs at the end of 3 h of reaction [15], we believe that the Fe and Pt atoms in these samples are the species that occur in the process of forming Fe@Pt NPs. The curves show striking contrasts between Fe and Pt yields. While the yield of Fe is high from the beginning of the reaction, the yield of Pt is very small initially. After 60 min, the yield of Pt picks up and sharply increases. The yield curve for Fe shows a decrease from 60 min and 90 min. The decrease of Fe yield between 60 and 90 min is concurrent with the increase of Pt yield, which may be interpreted as the signature of the galvanic displacement reaction between Fe NPs with $Pt(acac)_2$ depositing Pt and losing a part of Fe from Fe NPs. The XRD patterns of these samples in Fig. 3b show that the diffraction peaks for Fe@Pt NPs start to appear from the sample at 75 min, in agreement with this interpretation. The gradual increases of both Fe and Pt yields after 90 min can be understood as the continued formation of Fe@Pt NPs. In either way, the sharp rise of Pt yield at after 60 min and a continuous increase afterward along with that of Fe agree with the proposed mechanism for the Fe@Pt core–shell structure.

Because this reaction was run without carbon support, the appearances of the solution could be matched with the above analysis results

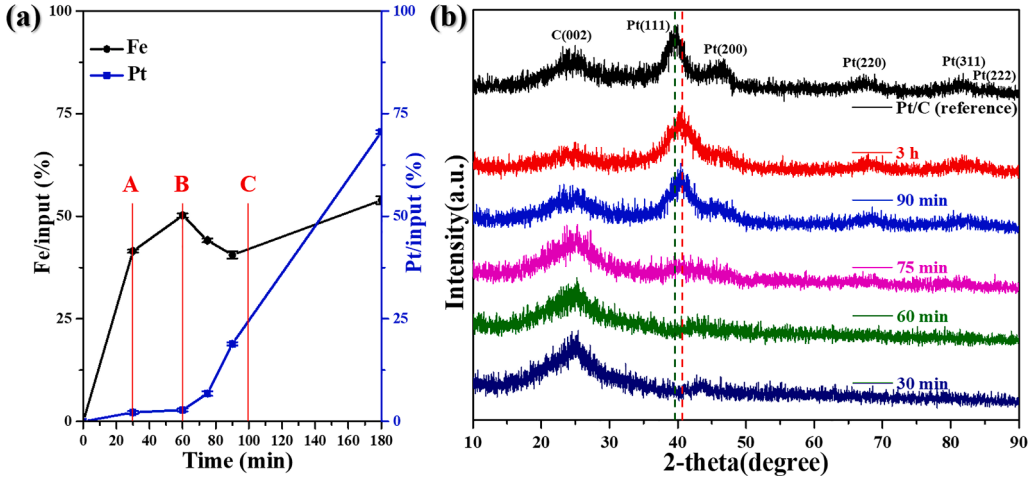

Fig. 3. Analysis results on 5 mL aliquots taken during a UPS reaction between $Fe(acac)_3$ and $Pt(acac)_2$ in EG triplicated in reaction scale (90 mL). (a) Time-variations of Fe and Pt contents in the aliquots with respect to the initial contents and (b) variation of XRD patterns with time of materials collected on KB. The data points in (a) are the averaged values of five different measurements.

(Figure S8), which enabled us to identify the solution state (states A, B, and C in Fig. 1) by visually inspecting the solution appearance. Accordingly, state A corresponds to a state in which a small amount of Fe NPs are formed in addition to the complete dissolution of both Fe- and Pt-reagents. State B corresponds to the point at which a large fraction of $Fe(acac)_3$ is converted to Fe NPs but the majority of $Pt(acac)_2$ has not yet reacted. Finally, in state C, the formation of Pt-shell to in Fe@Pt NPs has progressed to a certain extent, not the onset of the formation of Pt-shell. In fact, the formation of Pt shell appears to start between 60 and 75 min of reaction to see the small Pt-like peak in the XRD pattern of the 75 min sample. Apparently, it takes a certain amount of Fe@Pt NPs to be accumulated before the solution color turns into black.

3.5. Effects of ultrasonication condition

The amplitude of a sonicator is an important parameter to be considered for a ultrasonication reaction. The amplitude is defined as the amplitude of vibration of the sonicator horn relative to the maximum amplitude of the transducer which is predetermined for a given size of ultrasonication horn by the power of the transducer. For the case of $\phi =$ 13 mm horn, used in the present study, the maximum (100%) amplitude is 61 μm. Typically 20 – 30% of amplitude is used in most of literature works. If too high amplitude is used, the horn is damaged from the friction with the solution and the heat, shortening its life time. The erosion of the horn material may contaminate the reaction products with Ti and V, the major component of the sonicator horn [37,38]. The power delivered to the solution was calculated by using the equation proposed by Nikitenko et al. [39] as shown below:

$$I = \frac{\Delta T}{\Delta \tau}\frac{mQ}{S}$$

where $\Delta T/\Delta\tau$ is the initial heating rate (in °C min^{-1}), m is the mass of liquid (in g), Q is the specific heat of the liquid and S is the irradiative surface are of the horn (5.3 cm^2). In our case when EG ($Q = 2.43$ J g^{-1}) was used as the solvent, I is 2.26, 4.54, and 5.51 W cm^{-2} when the amplitude was 20, 25, and 30%, respectively.

When the amplitude is too low such as 20% instead of the 30% of all the reactions mentioned so far, the reaction between $Fe(acac)_3$ and $Pt(acac)_2$ does not show any sign of the formation of Fe@Pt NPs. On the other hand, when the amplitude is higher than 30%, the time to form Fe@Pt NPs can be shortened (Figure S9). Apparently, the ultrasonic

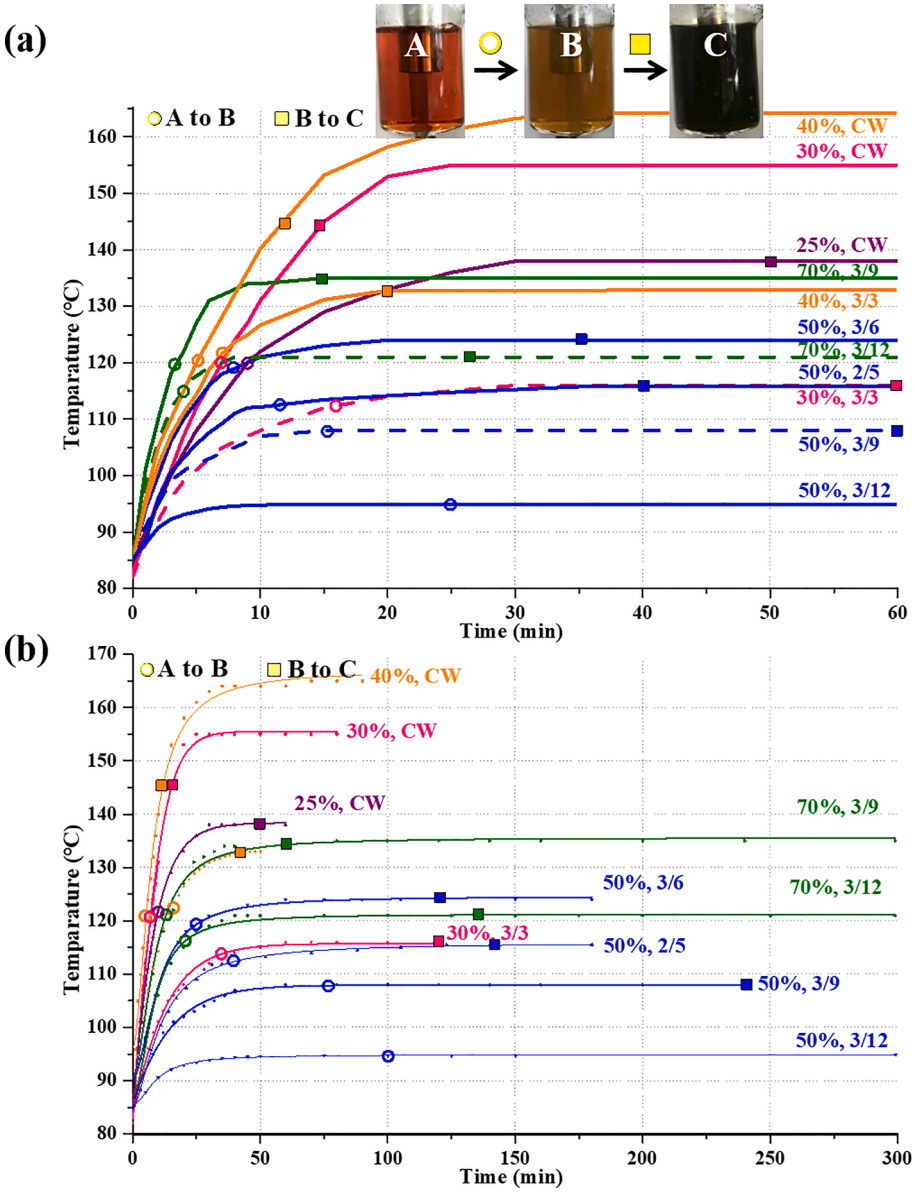

Fig. 4. Reaction progresses of the UPS reactions between $Fe(acac)_3$ and $Pt(acac)_2$ under various ultrasonication conditions. Both ultrasonication amplitude and on-and-off time condition are varied: (a) plots against the total (on-time + off-time) time and (b) plots against the net ultrasonication on-time. Vertical axes are the solution temperature. The label shows the ultrasonication amplitude and on/off time of ultrasonication. CW means continuous wave. Solution states A, B, and C (defined in the main text) are identified from the visual appearances of the ultrasolutions and are marked on each curve; circles are for the moments of state B is attained and squares are for the moments of state C.

power plays an important role in the reaction progress. However, these changes with the ultrasonication amplitude cannot be solely attributed to the amplitude effect because ultrasonication accompanies heating of the solution and different amplitude produces different rates of heating and different final temperatures of the solution.

In order to see the effects of temperature and ultrasonication power on the reaction progress, we ran some reactions with various combinations of ultrasonication amplitude and ultrasound on-and-off time (Fig. 4). In this figure, each curve is marked with the moments when states A, B, and C appear. The precision of the identification of the states is bound to have some errors because the identification was made visually. Nevertheless, these data can provide valuable information on the mechanism of the UPS reaction, as can be appreciated in the following discussion. The data are plotted in two different ways, one against the net ultrasonication time excluding the time when ultrasonication is turned off (Fig. 4a) and the other against the total time (Fig. 4b).

We will first discuss on the time of the transition from state A to state B, viz. from a complete solution to the state where Fe NPs without Pt shells are the major product. In the plot against the net ultrasonication time (Fig. 4a), although there appears a general tendency to take longer time for the state B to appear as the solution temperature becomes lower, there are a few deviations. For instance, the state B under 70% 3/12 condition appears at a lower temperature than the others of comparable temperature profiles such as 50% 3/6 and 40% CW conditions. The time required for state B to appear under 30% 3/3 condition is longer than under 50% 2/5 condition of the same final temperature. By contrast, in the plot against the total time spent (Fig. 4b), these deviations disappear and all the data points follow the above-mentioned general tendency. These observations manifest the temperature-dependent nature of the process involved in the formation of Fe NPs.

In an attempt to differentiate the effects of ultrasonication from the effects of temperature, some selected reactions were analyzed for the temperature dependence of the time for the transition from state A to state B ($time_{A\rightarrow B}$) by plotting $-\ln time_{A\rightarrow B}$ against 1/temperature graphs (Fig. 5). We selected the reactions run under 50% of amplitude with various combinations of on and off times. In this way, the effects of changing amplitude can be removed. In the plot in Fig. 5a, the net ultrasonication time was used for $time_{A\rightarrow B}$, and total time for the plot in Fig. 5b. The temperatures in these plots are the temperatures at which state B appears. Admittedly, this kind of plot cannot be considered to be as Arrhenius type because the temperature during the transition changes. Notwithstanding, that the plot using net ultrasonication time produces a linear relationship, but the one using total time does not suggest that the effect of ultrasonication has some direct effects to the formation of Fe NPs.

We interpret these findings as that the formation of Fe NPs involves the radicals generated from the implosion of bubbles during ultrasonication. In the following equations, we show an example of reaction between $Fe(acac)_3$ molecules and HO· radicals to form Fe NPs.

$$n\ Fe(acac)_3 + 3n\ HO \rightarrow Fe_n + 3n\ H_2O + 3\ H_3CCOCCOCH_3 \quad (9)$$

$$H_2O \rightarrow H\cdot + HO \quad (10)$$

$$3m\ Pt(acac)_2 + Fe_{2m} \rightarrow 2\ m\ Fe^{3+} + Pt_m \quad (11)$$

A close inspection of the data for the occurrence of state B suggests it depends on the heating rate (or temperature). When the heating rate is lower so that the amount of time required to reach 120 ℃ is long or this temperature is never reached, the above-mentioned inverse relation between the time of occurrence of state B and temperature appears to hold. On the contrary, when the heating rate is very high, it seems that state B appears when the solution temperature reaches ~ 120 ℃ regardless of the ultrasonication condition. We suspect that it is partly related with the change of viscosity of EG with temperature. EG is highly viscous with the room temperature viscosity of 15.5 cP. As the temperature increases, its viscosity decreases drastically to 1.8 cP at 116 ℃. [40] Because the size of bubbles is inversely related with the viscosity, it seems that a certain critical viscosity is required to produce sufficient amount of Fe NPs.

The progression from state B to state C also seems to depend on the temperature, more than on the ultrasonication power. To clearly show this, we selected the reactions in which the temperatures for state B and state C are close to each other so that the B → C transition can be regarded as an isothermal process, in which case, a plot of $-\ln time_{A\rightarrow B}$ against 1/temperature can be considered as an Arrhenius plot. Two $-\ln (time)_{B\rightarrow C}$ vs 1/T plots, one using the net ultrasonication time and the other total time, are compared in Fig. 6. While the plot using the total time give a straight line ($R^2 = 0.983$), the one using the net ultrasonication time does not ($R^2 = 0.853$). Evidently, the process of forming Pt shell on Fe NPs to form Fe@Pt NPs is a thermally activated process, consistent with the proposed galvanic displacement reaction between $Pt(acac)_2$ and Fe^0 on the surface of Fe NPs as in the originally proposed mechanism.

Because the instantaneous temperature at the event of bubble collapse is as high as 5,000 K, much higher than that of surrounding liquid medium, any reaction that occurs as a direct consequence of bubble collapse is likely to have little sensitivity to the temperature of the liquid medium. In this sense, none of the reactions involving metal species in the present UPS system is directly related with the bubble collapse. Rather, it seems that the radicals generated from the bubble collapse are the principal source of the reactions, in agreement with the

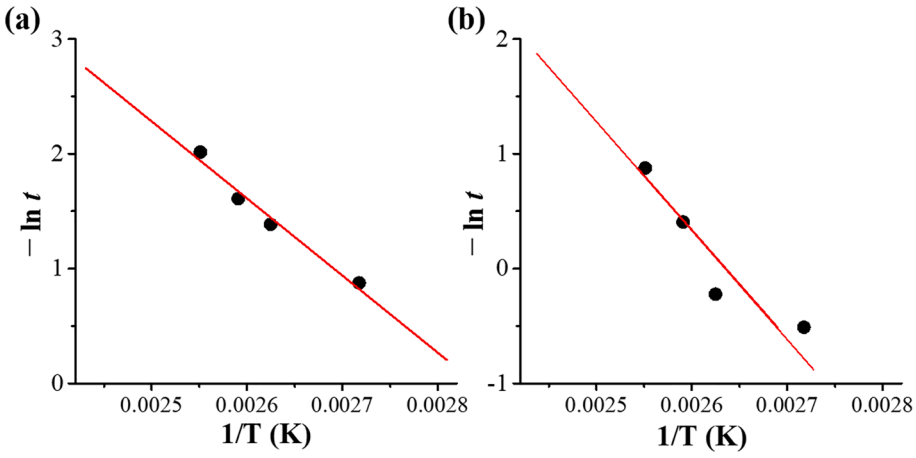

Fig. 5. Pseudo-Arrhenius ($-\ln (time)_{A\rightarrow B}$ vs 1/T) plots for the transition from state A to state B for reactions under 50% amplitudes with various ultrasonication on and off times. (a) Plot for net ultrasonication time and (b) plot for total time.

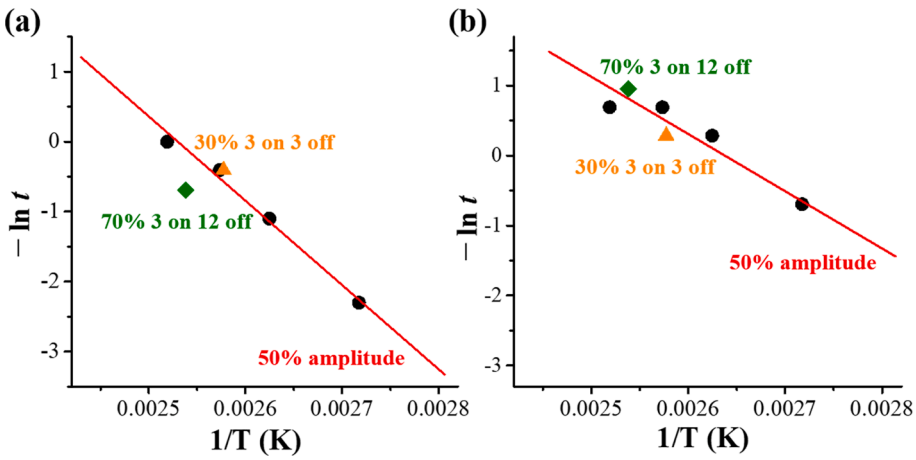

Fig. 6. Arrhenius (– ln (time)$_{B\rightarrow C}$ vs 1/T) plots of selected reactions from Fig. 4 for the transition from state B to state C. (a) Plots using the total times and (b) plot using the net ultrasonication time between state B and state C.

acoustic cavitation mechanism for sonochemistry.

Assuming that the dynamics of growing bubbles do not change drastically with the ultrasonication power, the amplitude is related with the rate of the formation of primary radicals. Of course, the diffusion of radicals is slower than the rate of radical formation especially when the power is very high. With the temperature increases, the diffusion rate also increases, more or less balancing with the rate of radical formation. In this sense, the amplitude of sonicator is not a critical parameter as long as the temperature can be maintained by some other means such as higher insulation of the reaction vessel or an externally supplied heat and the amount of radical production is sufficient.

In the foregoing discussions, we showed that temperature is an important parameter that governs the whole reaction during UPS process. The formation process of Fe NPs is dependent on the temperature of solution while the main driving mechanism is the implosion of bubbles providing primary and secondary radicals. The following process of forming Pt shell is the galvanic displacement reaction between Fe^0 atoms on the surface of Fe NPs and $Pt(acac)_2$, whose reaction rate follows the Arrhenius law. It needs to noted, however, that too high temperature has a detrimental effect in the synthesis of Fe@Pt NPs. In reactions where the final temperature exceeds 160 ℃, the resultant NPs become inhomogeneous in size. There are NPs as large as 4 or 5 nm which are absent in the products of reactions with the final temperature lower than 160 ℃. In addition, there are also very small (less than2 nm) NPs in the products, which is a signature of Fe-less or pure Pt NPs (Figure S10). Apparently, under a condition of too high temperatures, a reduction pathway of $Pt(acac)_2$ into Pt^0 other than the galvanic displacement between Fe^0 and $Pt(acac)_2$ is facilitated, which is likely to be the reaction with the secondary radicals.

3.6. *Refined mechanism*

Based on the observations discussed above and the existing theory on sonochemistry, we propose a revised reaction mechanism for the formation of Fe@Pt NP is schematically summarized in Scheme 1.

This mechanism is similar with the originally proposed one except for a few important points: First, instead of formaldehyde in eqn. 1, radicals are the principal reducing agent that form Fe NPs. Second, in addition to the galvanic displacement of Fe^0 atoms on Fe NPs by $Pt(acac)_2$ to be the sole mechanism to form Pt-shell, in the originally proposed mechanism, we include the reaction of $Pt(acac)_2$ with secondary radicals on Fe NP surface as another pathway. The reaction between $Pt(acac)_2$ and secondary radical gives another pathway that may be a source of undesirable Pt NPs free from Fe cores.

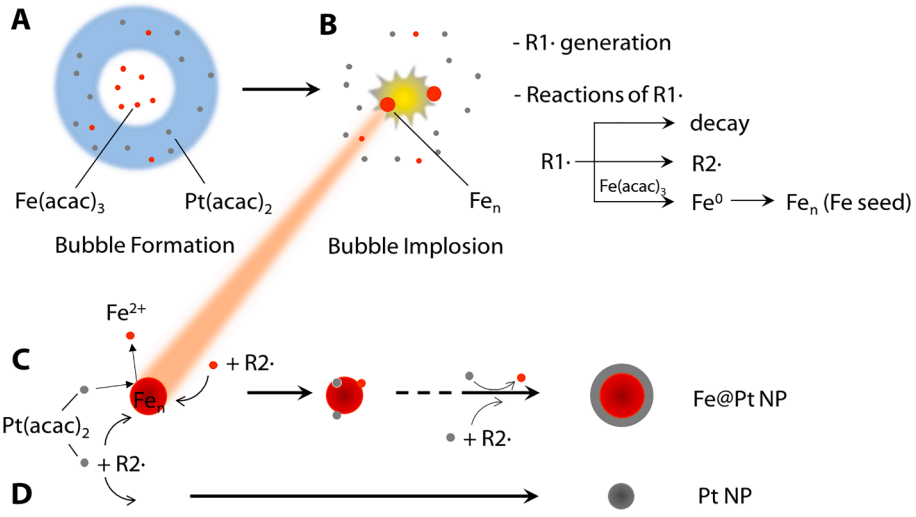

Scheme 1. Revised proposed mechanisms of chemical reactions during sonochemical reaction between $Fe(acac)_3$ and $Pt(acac)_2$ in EG: (A) Bubbles are formed and grow through in size. Volatile $Fe(acac)_3$ molecules are accumulated inside the bubble while nonvolatile $Pt(acac)_2$ molecules stay outside of the bubbles. (B) When bubbles implode, the high energy pulse accompanying the bubble implosion induces the bond breaking of $Fe(acac)_3$ and EG molecules accumulated inside the bubbles. Primary radicals (R1·) are and Fe^0 atoms are formed. While a large part of R1· is lost by decaying, some generate secondary radicals (R2) and also Fe^0 atoms through the reaction with Fe $(acac)_3$. Fe^0 atoms grow into Fe_n (Fe seed). (C) Fe seeds undergo three major reactions: Deposition of Fe^0 atoms through the reaction between $Fe(acac)_3$ and R2·, deposition of Pt^0 atoms through galvanic displacement reaction with Fe^0 atoms on the surface and through the reaction between $Pt(acac)_2$ and R2·. The reaction of Fe seed is stopped when the whole surface is covered by Pt atoms to make Fe@Pt core–shell structure. (D) The reaction between $Pt(acac)_2$ and R2· can also form Pt^0 atoms independent of Fe seeds, resulting in Pt nanoparticles.

Based on the mechanism, Fe NPs are mainly formed immediately after the bubble implosion which may be affected by the ultrasonication power which can be controlled by the controlling the amplitude of the sonicator horn. On the contrary, the formation of Pt-shell or Pt NPs is a chemically driven process which is subject to the influence of the temperature of the solution. In a typical ultrasonication reaction, the solution is naturally heated. Therefore, the control of the amplitude actually controls both the amount of power delivered by the ultrasonication and the temperature. In order to finely control the reaction, it may be necessary to control the ultrasonication power and temperature separately. It might be that the successful formation of Fe@Pt NPs in a typical small-scale synthesis happened to have both the power and temperature in the right conditions.

4. Conclusions

In this study, we performed detailed studies on the reaction mechanism for the formation of Fe@Pt NPs through UPS reaction. The observation of fragments of EG by GC–MS indicate that the acoustic cavitation mechanism, usually explained for aqueous solutions, apply to the present system using EG as the solvent. The counterintuitive claim that $Fe(acac)_3$ reacts before $Pt(acac)_2$ under UPS condition despite that the latter is more prone to reduction reaction is verified by analyzing the materials obtained in the course of the reaction progress. The higher reactivity of $Fe(acac)_3$ than $Pt(acac)_2$ is explained as the accumulation of $Fe(acac)_3$ molecules inside the bubbles formed by ultrasonication through vaporization. On the other hand, through the comparison with insoluble PtO_2, it is shown that the solubility of $Pt(acac)_2$ plays an important role in the formation of Pt shell. These detailed understandings on the reaction mechanism will be able to open possibilities to control reactions more precisely. At present, we are trying to apply this knowledge in increasing the reaction scale so that our UPS synthesis of Fe@Pt/C catalyst can have more direct application in industry.

CRediT authorship contribution statement

Ah-Hyeon Park: Investigation, Data curation, Writing - original draft. **Wenjuan Shi:** Investigation. **Jong-Un Jung:** Investigation. **Young-Uk Kwon:** Funding acquisition, Writing - review & editing.

Declaration of Competing Interest

The authors declare that they have no known competing financial interests or personal relationships that could have appeared to influence the work reported in this paper.

Acknowledgements

This work was supported by Industry-University Cooperation Research Program through the Hyundai NGV Company of Korea. We thank Mr. Byeong-Jun Cha and Prof. Young-Dok Kim for the GC-MS measurements.

Appendix A. Supplementary data

Supplementary data to this article can be found online at https://doi.org/10.1016/j.ultsonch.2021.105679.

References

[1] R. Wang, H. Wang, F. Luo, S. Liao, Core–shell-structured low-platinum electrocatalysts for fuel cell applications, Electrochem. Energy Rev. 1 (3) (2018) 324–387.
[2] X. Ren, Q. Lv, L. Liu, B. Liu, Y. Wang, A. Liu, G. Wu, Current progress of Pt and Pt-based electrocatalysts used for fuel cells, Sustainable Energy Fuels 4 (1) (2020) 15–30.
[3] P. Wang, Q.i. Shao, X. Huang, Updating Pt-based electrocatalysts for practical fuel cells, Joule 2 (12) (2018) 2514–2516.
[4] A. Kulkarni, S. Siahrostami, A. Patel, J.K. Nørskov, Understanding catalytic activity trends in the oxygen reduction reaction, Chem. Rev. 118 (5) (2018) 2302–2312.
[5] J. Huang, M. Eikerling, Modeling the oxygen reduction reaction at platinum-based catalysts: a brief review of recent developments, Curr. Opin. Electrochem. 13 (2019) 157–165.
[6] C. Zhang, X. Shen, Y. Pan, Z. Peng, A review of Pt-based electrocatalysts for oxygen reduction reaction, Front. Energy 11 (2017) 268–285.
[7] K. Kodama, T. Nagai, A. Kuwaki, R. Jinnouchi, Y. Morimoto, Challenges in applying highly active Pt-based nanostructured catalysts for oxygen reduction reactions to fuel cell vehicles, Nat. Nanotechnol. 16 (2021) 140–147.
[8] B.G. Pollet, I. Staffell, J.L. Shang, Current status of hybrid, battery and fuel cell electric vehicles: From electrochemistry to market prospects, Electrochim. Acta 84 (2012) 235–249.
[9] F.H.B. Lima, J. Zhang, M.H. Shao, K. Sasaki, M.B. Vukmirovic, E.A. Ticianelli, R. R. Adzic, Catalytic Activity−d-Band Center Correlation for the O2 Reduction Reaction on Platinum in Alkaline Solutions, J. Phys. Chem. C 111 (2007) 404–410.
[10] S.J. Hwang, S.J. Yoo, J. Shin, Y.H. Cho, J.H. Jang, E. Cho, Y.E. Sung, S.W. Nam, T. H. Lim, S.C. Lee, S.K. Kim, Supported core@shell electrocatalysts for fuel cells: close encounter with reality, Sci. Rep. 3 (2013) 1309.
[11] G.R. Chaudhuri, S. Paria, Core/shell nanoparticles: classes, properties, synthesis mechanisms, characterization, and applications, Chem. Rev. 112 (4) (2012) 2373–2433.
[12] M.B. Gawande, A. Goswami, T. Asefa, H. Guo, A.V. Biradar, D.-L. Peng, R. Zboril, R.S. Varma, Core-shell nanoparticles: synthesis and applications in catalysis and electrocatalysis, Chem. Soc. Rev. 44 (21) (2015) 7540–7590.
[13] E. Lee, Y.-U. Kwon, Multi-component electrocatalyst for low-temperature fuel cells synthesized via sonochemical reactions, Ultrason. Sonochem. 29 (2016) 401–412.
[14] J.-H. Jang, J. Kim, Y.-H. Lee, I.Y. Kim, M.-H. Park, C.-W. Yang, S.-J. Hwang, Y.-U. Kwon, One-pot synthesis of core–shell-like Pt3Co nanoparticle electrocatalyst with Pt-enriched surface for oxygen reduction reaction in fuel cells, Energy Environ. Sci. 4 (12) (2011) 4947–4953, https://doi.org/10.1039/c1ee01825f.
[15] J.H. Jang, E. Lee, J. Park, G. Kim, S. Hong, Y.U. Kwon, Rational syntheses of core-shell Fex@Pt nanoparticles for the study of electrocatalytic oxygen reduction reaction, Sci. Rep. 3 (2013) 2872.
[16] E. Lee, J.H. Jang, M.A. Matin, Y.U. Kwon, One-step sonochemical syntheses of Ni@Pt core-shell nanoparticles with controlled shape and shell thickness for fuel cell electrocatalyst, Ultrason. Sonochem. 21 (2014) 317–323.
[17] H.U. Park, A.H. Park, W. Shi, G.G. Park, Y.U. Kwon, Ternary core-shell PdM@Pt (M=Mn and Fe) nanoparticle electrocatalysts with enhanced ORR catalytic properties, Ultrason. Sonochem. 58 (2019), 104673.
[18] D.S. Karousos, K.I. Desdenakis, P.M. Sakkas, G. Sourkouni, B.G. Pollet, C. Argirusis, Sonoelectrochemical one-pot synthesis of Pt - Carbon black nanocomposite PEMFC electrocatalyst, Ultrason Sonochem 35 (2017) 591–597.
[19] B. Pollet, The use of power ultrasound for the production of PEMFC and PEMWE catalysts and low-Pt loading and high-performing electrodes, Catalysts 9 (2019) 246.
[20] B.G. Pollet, S.S. Kocha, Using ultrasound to effectively homogenise catalyst inks: Is this approach still acceptable? Johnson Matthey Technol. Rev. (2021) https://doi.org/10.1595/205651321X16196162869695.
[21] F. Foroughi, J.J. Lamb, O.S. Burheim, B.G. Pollet, Sonochemical and sonoelectrochemical production of energy materials, Catalysts 11 (2) (2021) 284, https://doi.org/10.3390/catal11020284.
[22] B.G. Pollet, The use of ultrasound for the fabrication of fuel cell materials, Int. J. Hydrogen Energy 35 (2010) 11986–12004.
[23] J.I. Park, M.G. Kim, Y.W. Jun, J.S. Lee, W.R. Lee, J. Cheon, Characterization of superparamagnetic "core-shell" nanoparticles and monitoring their anisotropic phase transition to ferromagnetic "solid solution" nanoalloys, J. Amer. Chem. Soc. 126 (2004) 9072–9078.
[24] B.D. Fahlman, A.R. Barron, Substituent effects on the volatility of metal, Adv. Mater. Opt. Electron 10 (2000) 223–232.
[25] J.R.V. Garcia, T. Goto, Chemical vapor deposition of iridium, platinum, rhodium and palladium, Mater. Trans. 44 (2003) 1717–1728.
[26] M.A. Matin, J. Lee, G.W. Kim, H.-U. Park, B.J. Cha, S. Shastri, G. Kim, Y.D. Kim, Y. U. Kwon, V. Petkov, Morphing Mn_{core}@ Pt_{shell} nanoparticles: Effects of core structure on the ORR performance of Pt shell, Appl. Catal. B: Environ. 267 (2020), 118727.
[27] V. Petkov, B. Prasai, S. Shastri, H.U. Park, Y.U. Kwon, V. Skumryev, Ensemble averaged structure-function relationship for nanocrystals: effective superparamagnetic Fe clusters with catalytically active Pt skin, Nanoscale 9 (2017) 15505–15514.
[28] J. Chen, B. Yao, C. Li, G. Shi, An improved Hummers method for eco-friendly synthesis of graphene oxide, Carbon 64 (2013) 225–229.
[29] F. Fievet, J.P. Lagier, B. Blin, B. Beaudoin, M. Figlarz, Homogeneous and heterogeneous nucleations in the polyol process for the preparation of micron and submicron size metal particles, Solid State Ionics 32–33 (1989) 198–205.
[30] R.J. Joseyphus, K. Shinoda, D. Kodama, B. Jeyadevan, Size controlled Fe nanoparticles through polyol process and their magnetic properties, Mater. Chem. Phys. 123 (2010) 487–493.
[31] K.S. Suslick, Y. Didenko, M.M. Fang, T. Hyeon, K.J. Kolbeck, W.B.M. III, M.M. Mdleleni, M. Wong, Acoustic cavitation and its chemical consequences, Phil. Trans. R. Soc. Lond. A, 357 (1999) 335–353.
[32] K.S. Suslick, G.J. Price, Applications of ultrasound to materials chemistry, Annu. Rev. Mater. Sci. 29 (1999) 295–326.

[33] E. Lee, A.H. Park, H.U. Park, Y.U. Kwon, Facile sonochemical synthesis of amorphous NiFe-(oxy)hydroxide nanoparticles as superior electrocatalysts for oxygen evolution reaction, Ultrason. Sonochem. 40 (2018) 552–557.
[34] E. Lee, J.H. Jang, Y.U. Kwon, Composition effects of spinel $Mn_xCo_{3-x}O_4$ nanoparticles on their electrocatalytic properties in oxygen reduction reaction in alkaline media, J. Power Sources 273 (2015) 735–741.
[35] B.S. Lim, A. Rahtu, J.-S. Park, R.G. Gordon, Synthesis and Characterization of Volatile, Thermally Stable, Reactive Transition Metal Amidinates, Inorg. Chem. 42 (2003) 7951–7958.
[36] A.G. Starikov, D.G. Ivanov, A.A. Starikova, V.I. Minkin, Dispersion interactions in oligomerization of metal diketonates: a DFT evaluation, Chem. Pap. 72 (4) (2018) 829–839.
[37] H.E. Hansen, F. Seland, S. Sunde, O.S. Burheim, B.G. Pollet, Two routes for sonochemical synthesis of platinum nanoparticles with narrow size distribution, Mater. Adv. 2 (6) (2021) 1962–1971.
[38] Y.O. Kenji, T. Shuji, M. Hiroshige, Y. Yoshihiro, Y. Yoo, Sonolytic control of rate of gold(III) reduction and size of formed gold nanoparticles: relation between reduction rates and sizes of formed nanoparticles, Bull. Chem. Soc. Jpn. 75 (10) (2002) 2289–2296.
[39] S.I. Nikitenko, P. Moisy, A.F. Seliverstov, P. Blanc, C. Madic, Sonolysis of metal b-diketonates in alkanes, Ultrason. Sonochem. 10 (2003) 95–102.
[40] T. Sun, A.S. Teja, Density, viscosity, and thermal conductivity of aqueous ethylene, diethylene, and triethylene glycol mixtures between 290 K and 450 K, J. Chem. Eng. Data 48 (1) (2003) 198–202.